Research Square

Preprints are preliminary reports that have not undergone peer review.
They should not be considered conclusive, used to inform clinical practice,
or referenced by the media as validated information.

Constant Potential Electrochemistry with Multiscale Quantum Mechanical / Machine Learning Simulations

Seung-Jae Shin

seungjae.shin@unist.ac.kr

Ulsan National Institute of Science & Technology https://orcid.org/0000-0002-5530-4453

Aron Walsh

Imperial College London https://orcid.org/0000-0001-5460-7033

Kara Fong

Caltech

Article

Keywords:

Posted Date: June 16th, 2026

DOI: https://doi.org/10.21203/rs.3.rs-9960795/v1

License: This work is licensed under a Creative Commons Attribution 4.0 International License.
Read Full License

Additional Declarations: There is **NO** Competing Interest.

Constant Potential Electrochemistry with Multiscale Quantum Mechanical / Machine Learning Simulations

Seung-Jae Shin[1*], Kara D. Fong[2], and Aron Walsh[3]

[1] *School of Energy and Chemical Engineering, Ulsan National Institute of Science and Technology (UNIST), Ulsan 44919, Republic of Korea*
[2] *Division of Chemistry and Chemical Engineering, California Institute of Technology, Pasadena, CA 91125, USA*
[3]*Department of Materials, Imperial College London, Exhibition Road, SW7 2AZ, London, United Kingdom*

*e-mail: seungjae.shin@unist.ac.kr

ABSTRACT: Deeper theoretical understandings of electrified interfaces become important for the development of electrochemical devices. While much progress has been in computational electrochemistry, constant-potential-simulations pose fundamental challenges. Here, we report a multiscale quantum-mechanical/machine-learning (QM/ML) approach, effectively reducing the computational time, but maintaining the accuracy of QM with an explicit description of the electrolyte components. Implementation of a bias potential to the electrodes, maintained with a bespoke computational potentiostat, allows the system to achieve the constant potential (μVT) ensemble. Charging dynamics and electrolyte response show a one-to-one correlation in the pure water but not in the ionic system. Lager electrolytes lead to a longer convergence timescale of interfacial polarization due to greater configurational entropy, yet remains consistent in generating μVT ensemble. Without employing the

potentiostat, the potential exhibits significant fluctuations reinforcing its necessity. Multiscale embedding theory that takes advantage of increasingly powerful machine learning surrogate models offers a promising avenue to model realistic electrochemical systems.

MAIN

Electrochemical interfaces are a cornerstone of modern energy technology, fundamentally underpinning the performance of devices such as batteries, fuel cells, and (photo-)electrochemical cells[1]. Developing a sustainable and renewable energy-based society necessitates a deep atomic-level understanding of electrified interfaces to rationally design materials and systems to optimize reaction mechanisms.

Theoretical investigations have been crucial in elucidating interfacial structures and reaction pathways. Early advances relied on the computational hydrogen electrode (CHE) model to predict reaction energetics across diverse materials[2]. Subsequent efforts integrated implicit or explicit double-layer models into density functional theory (DFT), allowing for electrode charging and reinforcing the CHE framework[3–5]. Ab initio molecular dynamics (AIMD) simulations have significantly advanced computational electrochemistry. They provide profound insights into the electrochemical interface by employing constant charge ensembles, coupling to mean-field models, or explicitly charging solvent molecules[6–10]. Due to their high computational cost, various alternative approaches have been developed, such as multiscale Quantum Mechanics/Molecular Mechanics (QM/MM) and machine learning force fields (MLFFs)-based MD simulations[3,11–13]. However, simulating the interface under experimental conditions remains a major challenge. While recent progress has focused on developing constant potential methods[14,15], these often neglect the explicit structure of the double layer due to prohibitively high computational costs. While methods based on classical electrostatics and AIMD have been previously reported[16–18], there still remains a need for an

ab initio quality approach that explicitly accounts for electrolyte structure at an affordable computational cost.

Investigating electrochemical interfaces within confined spaces is crucial. From a practical perspective, the rapid development of nanomaterials has highlighted the significance of sub-nanoscale phenomena in various applications, such as batteries and electrocatalysts[19]. Theoretically, conventional models like the Gouy-Chapman-Stern (GCS) theory often fail to accurately describe behavior at these scales[20–22]. However, due to the extreme difficulties of experimental measurement, these interfaces remain largely unexplored. While recent studies have begun to examine related interfacial structures, many have yet to fully account for the complexities of the electrified interface[23–26].

Herein, we introduce a multiscale quantum mechanical / machine learning (QM/ML) simulation methodology coupled with a computational potentiostat to execute constant potential (μVT) ensemble simulations. While conventional MLFFs offer DFT-comparable accuracy for short-range interactions, they struggle to accurately capture the long-range electrostatic (ES) potentials critical to electrochemical systems[13]. We address this by employing an ES embedding scheme within the QM/ML framework, where particles are treated with either DFT or an MLFF and assigned point charges. The non-ES potential is trained using an ML architecture, assuming the non-ES potential decays in the short range[27]. Furthermore, a bias potential is applied to the electrodes, which serves as the computational potentiostat.

We apply this methodology to a case study of graphene bilayers incorporating monolayer water molecules to investigate electrified interface dynamics at the sub-nanoscale.

Across the investigated potential range of 0–1.5 V, the resultant potential converges to the target value within ~2 ps, but exhibits large fluctuations without using potentiostat, further reinforcing its necessity. The charging dynamics and the electrolyte response exhibit a strong correlation. We further validate its transferability to more realistic models, including a larger bilayer distance model and an ionic electrolyte system. It demonstrates the capability of this methodology for modelling electrochemical interfaces with deep microscopic insights.

RESULTS

Development of a constant-potential QM/ML

The embedding technique employed here deals with subsystems treated by different levels of theory, specifically DFT and ML (Figure 1a)[28]. ES embedding considers the interfacial interaction along the boundary using both ES and non-ES potentials. The ES potential is computed using DFT for particles in the QM region and point charges for those in the ML region. The non-ES potential is subsequently described via an MLFF, optimal for treating short-range interactions[29]. The training dataset for the MLFF is constructed by subtracting the ES potential from the original DFT dataset. This theoretical framework accurately captures the response of water monolayer to external potentials, showing excellent agreement with DFT results up to 2.5 V $Å^{-1}$. This range encompasses the electric field magnitudes employed to generate the μVT ensemble in this study (Figures 1b and 1c). Further details are provided in Supplementary Note 1. Moreover, given the inherent flexibility of MLFFs, they are expected to be less dependent on the point charge values than classical force fields, provided the training

dataset is sufficiently comprehensive and the charges remain within a physically reasonable range[30]. We demonstrated that consistent responses were obtained using two different point charge models for water molecules under a constant external field (Supplementary Notes 2).

This QM/ML approach offers distinct advantages over both QM/MM and AIMD. Unlike traditional QM/MM, which relies on non-reactive force fields with fixed bonding topologies, our ML-based model allows for the breaking and formation of chemical bonds. Furthermore, while QM/MM requires system-specific potentials, e.g., OPLS-AA for liquids or EAM for metals[31,32], QM/ML provides greater flexibility across diverse chemical environments without the need for manual potential re-parameterization. While AIMD is the gold standard for accuracy, it faces significant time and length scale limitations. The QM/ML approach effectively bypasses these constraints by achieving high computational efficiency while maintaining near-quantum accuracy. This scalability allows for the exploration of complex interfacial phenomena over longer trajectories and larger system sizes that are currently inaccessible to conventional AIMD (Supplementary Note 3).

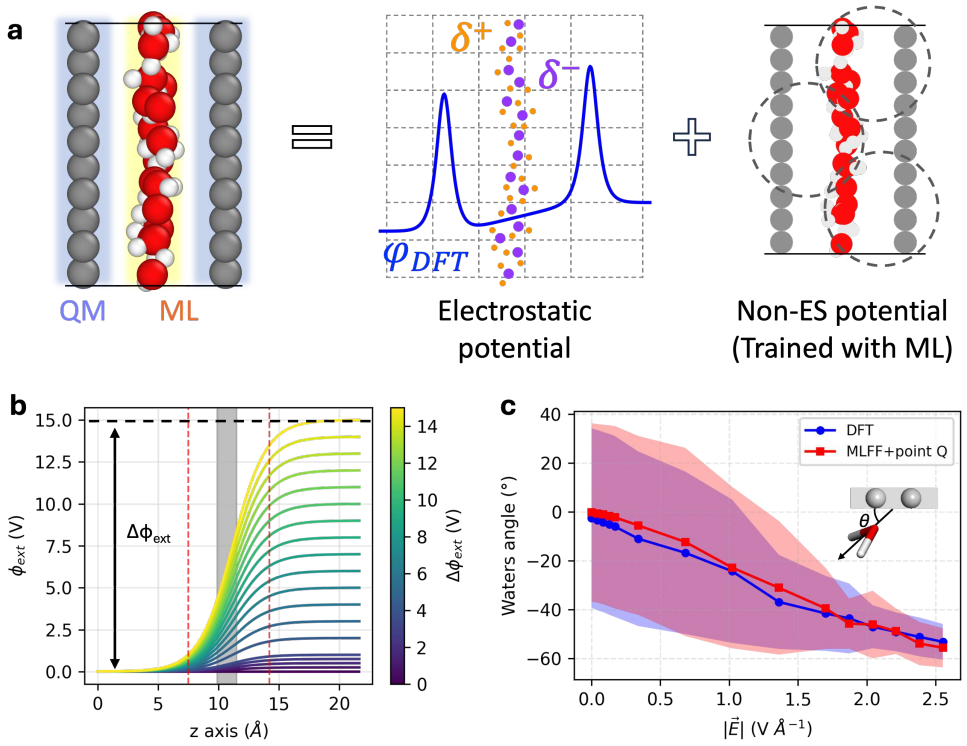


Figure 1. **a**, Schematic illustration of the multiscale QM/ML simulation methodology. The ES potential is calculated by conducting DFT for the QM region and assigning point charges for the ML region. The non-ES potential is then computed based on the MLFF to account for short-range interactions. **b,** The external potential profile, ϕ_{ext}, is shown for various potential differences, $\Delta\phi_{ext}$. The red dashed lines indicate the position of the graphene electrode during the QM/ML simulations. The grey shaded region indicates where the water monolayer exists. **c,** The average orientation angle of water molecules as a function of the magnitude of the electric field for the grey shaded region in panel **b**. The corresponding standard deviation is indicated by the shaded region. The angle is defined as that between the vector connecting the oxygen atom to the midpoint of the hydrogen atoms and the electrode surface.

A two-electrode configuration model enables simultaneous measurement of the ES potential at both the working electrode ($\bar{\varphi}_{\mathrm{work}}$) and the counter electrode ($\bar{\varphi}_{\mathrm{count}}$), which allows us to read the potential difference ($\Delta\Phi$) every timestep during the QM/ML simulations (Figure 2). The deviation from the target potential value (Φ_{set}) is recorded as Φ_{dev}. This approach is consistent with the principle of potentiometry used in experiments[33,34].

A three-electrode configuration is achievable within this theoretical framework and is planned to be implemented in future work. This extension will allow us to define the electrode potential on the Reversible Hydrogen Electrode (RHE) scale, enabling a direct match of the simulation results with experimental findings[9,10]. Since characterizing electrochemical interfaces in non-confined spaces is more accessible and better understood (e.g., in terms of interfacial capacitance[3,6–8,10]) this approach will not only validate our methodology but also provide insights into less-explored details, such as reaction dynamics under constant potential. However, a larger database will be necessary to extend this framework to complex and multi-scale phenomena like outer-sphere electron transfer or the diffuse layer, which were beyond the scope of the present study.

A bias potential is then applied to the electrodes (i.e., the graphene layers) to generate a μVT ensemble. The embedding approach is efficient for implementing this scheme as the electronic structure of the electrode and the electrolyte are clearly separated[35]. A sigmoid-shaped external potential with a magnitude of Φ_{dev} was employed to apply the bias potential to the electrodes. This controls the polarization of both electrodes such that the resultant potential difference ($\Delta\Phi'$) is expected to approach Φ_{set} with a reduced deviation (Φ'_{dev}). This

also parallels the operational principle of an experimental potentiostat[33,34]. We acknowledge that there are diverse ways to implement this potential control, as the role of the potentiostat is to generate the μVT ensemble. Our current scheme is specifically optimized for embedding theories. However, other frameworks—such as those based on the modern theory of polarization—could also be integrated in future work, given their broad applicability ranging from classical MD to AIMD[17,18]. Details of the theoretical architecture are described in the Methods section.

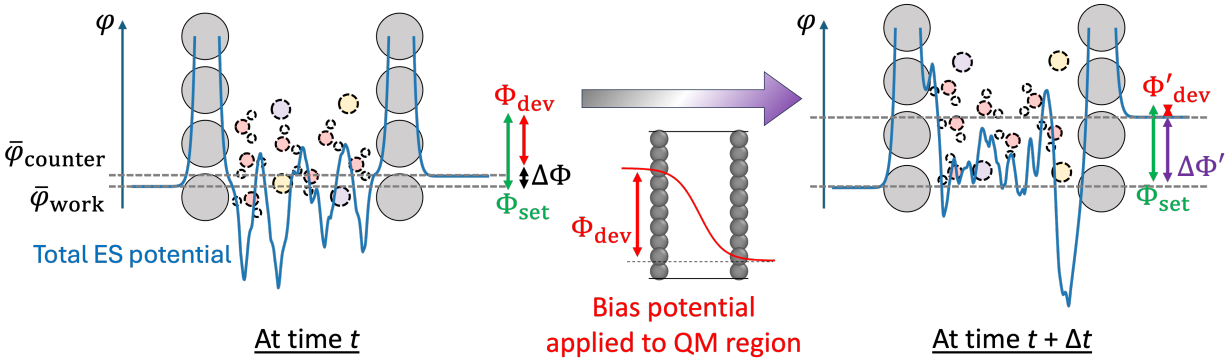


Figure 2. Schematic illustration for generating the μVT ensemble via multiscale QM/ML simulation. $\bar{\varphi}_{\mathrm{work}}$ is referenced to $\bar{\varphi}_{\mathrm{counter}}$ to define $\Delta\Phi$. Φ_{dev} is calculated iteratively by measuring the difference between $\Delta\Phi$ and Φ_{set}. A bias potential is then applied to adjust the potential difference to $\Delta\Phi'$, bringing it closer to Φ_{set} after time increment Δt.

Our approach distinguishes itself from standard MLFF frameworks in its treatment of ES interactions and electrode potential. A common strategy within the MLFF community

involves predicting environment-dependent atomic charges to accurately reproduce the electrostatic potential surface[36]. While we acknowledge these advancements in decoupling ES and non-electrostatic interactions, our current model employs a fixed-charge scheme. This does not imply that electronic polarization is neglected. There are two key mechanisms by which our framework captures polarization effects. First, the electronic structure of the electrode is fully polarizable, as it is treated at the QM level and responds to the local chemical environment. Second, although the electrolyte charges are fixed, the MLFF-predicted potential energy compensates for polarization effects not captured by the fixed-charge Coulombic term alone. This compensation is possible because, unlike classical fixed-charge models such as SPC/E, our water molecules retain full degrees of freedom in their bond lengths and angles, allowing the electronic response to vary with molecular geometry (Supplementary Note 2). This is justified by the relatively constant charge states observed in our system, where interfacial chemical reactions are absent[37].

Indeed, numerous studies employing fixed charge models within QM/MM framework have succeeded in quantitatively reproducing key electrochemical features, such as the camel-shaped and bell-shaped capacitance curves, using classical force field potentials such as the Lennard–Jones potential[3,38], and a similar framework combining fixed point charges with a trained MLFF remains actively used for understanding solid–liquid interfaces[37,39]. In light of the more accurate description offered by MLFF over classical potentials, and given that our MLFF is explicitly trained under applied potential conditions with a rigorous DFT-based treatment of the electrode electronic structure, our framework offers particular advantages for

studying electrochemical systems involving complex combinations of electrodes and electrolytes. However, this aspect can be further refined in future work by incorporating sophisticated charge-update schemes[36,40].

On the other hand, our scheme introduces a QM-based treatment for the electrode to maintain a constant potential and describe the interactions between the charged electrode and the electrolyte. A standard approach follows the classical electrodynamics[16], which has been recently augmented with MLFF[41]. This combined method offers high computational efficiency and results comparable to AIMD at the electrochemical interface. In contrast, our QM-coupled approach balances computational expense with physical fidelity, offering a robust interfacial description independent of the metallic character of the electrode. This enables in-depth insights into the electronic structure and realistic electrostatic potential profiles under electrochemical bias—features that remain challenging for purely classical or MLFF-based methods. We anticipate that this will be of particular interest to the community seeking to understand complex physicochemical phenomena at the electrochemical interface. This may include, for example, elucidating reaction mechanisms at electrodes with complex interfacial structures such as oxide surfaces and amorphous metallic electrodes.

Generation of constant potential ensemble

The initial DFT dataset was retrieved from a previous AIMD study[37]. Additional DFT calculations were then conducted to decouple the ES and non-ES potentials from this initial dataset. By approximating the electrolyte electrostatics as external point charges, DFT

calculations were performed on the graphene electrodes. The resultant non-ES dataset was subsequently employed to train the MLFF (Figure S1). The ensemble of seven MLFF models yielded sensible root mean square error (RMSE) values: energies of ~0.4 meV atom^{-1} and forces of ~35 meV Å^{-1}.

A μVT ensemble was initially generated using the QM/ML framework based on the initial dataset. Testing at $\Delta\Phi$ = 0.5 V revealed that within the seven-member committee of ML models, four models showed an RMSE for energy prediction up to ten times higher, i.e., 3.05 meV atom^{-1}. This increase occurred because the configurations became more diverse (out of distribution) compared to those without an applied potential (Figure S2). The test dataset for this validation was prepared by performing DFT calculations after the μVT ensemble generation.

Fine-tuning of the ML models was conducted using μVT ensembles where $\Delta\Phi$ was set to 0.5 V and 1.0 V. Consecutive DFT calculation and ES potential decoupling produced the next-generation training dataset. To bypass the issue of catastrophic forgetting, the new and initial datasets were merged during the training process[43]. This procedure ultimately resulted in a stable ML framework across the condition without a potentiostat (w.o. pot.) and the two different applied potential conditions (Figure S3). The largest RMSE for energy prediction across the seven committee models was 0.35 meV atom^{-1}.

Importantly, this MLFF proved transferable to different potential regimes that were not sampled directly during the training. To validate this, we examined four potential values (0.25, 0.75, 1.25, and 1.5 V), covering both smaller and larger $\Delta\Phi$ ranges than those in the

training set. In these cases, all models achieved an energy prediction RMSE of less than 0.5 meV atom^{-1} (Figures S4–6). The dissociation of water molecules was not considered in this work but this theoretical framework is transferable to various systems and should be useful for studying reaction dynamics under constant potential conditions as well[44,45].

The optimized potentiostat-implemented QM/ML framework successfully produced the μVT ensemble, covering ΔΦ ranges from 0.0 V to 1.5 V with 0.25 V increments. Similar to a barostat and thermostat[46–48], the potentiostat introduces fluctuations to the system, but the averaged ΔΦ values are well-produced and match the target values (Figure 3a and Figure S7). The magnitude of the fluctuation will be dependent on the simulation setup, but here it was approximately 0.25 V.

The timescale for achieving potential convergence, τ_{Φ}, was found to be less than 10 ps within the investigated potential range (Figure 3b). At ΔΦ = 0.0 V and 0.25 V, τ_{Φ} was nearly zero, indicating a smooth transition from the state where the potentiostat is inactive. Interestingly, as ΔΦ increased from 0.75 V to 1.5 V, τ_{Φ} decreased from 2 ps to 1 ps, suggesting that higher ΔΦ facilitates a faster generation of the μVT ensemble. Notably, at ΔΦ = 0.5 V, the total τ_{Φ} comprised two distinct timescales: $\tau_{\Phi,1}$ and $\tau_{\Phi,2}$. Up to t = $\tau_{\Phi,1}$, the system exhibited a smooth transition similar to that observed below 0.25 V. However, ΔΦ showed significant fluctuations during $\tau_{\Phi,2}$ before converging to 0.5 V, a behavior also seen above 0.75 V. A detailed mechanism will be discussed below. Since $\tau_{\Phi,2}$ was 2 ps, it can be inferred that

potential convergence typically occurs within 2 ps in this monolayer system once a response is initiated.

An important observation from this approach is that simulations with no potentiostat (nominally unbiased) produce different results from those held at 0 V. While the averaged value across a long timescale (> 150 ps in this work) approaches 0.0 V, the standard approach results in large fluctuations of more than 0.5 V. This trajectory is fundamentally different from the 0.0 V μVT ensemble, which consistently yields a converged average value. While it is generally assumed that a neutral interface simulated using standard molecular dynamics will inherently give the 0.0 V condition, this is not necessarily true for polar systems, and the resulting ensemble must be properly inspected.

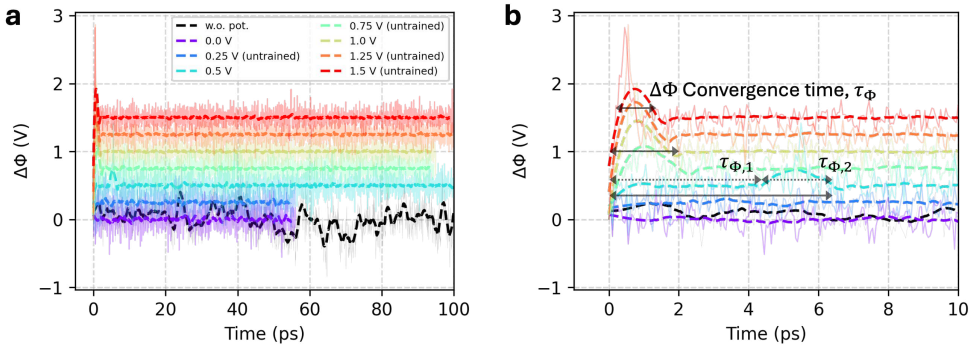


Figure 3. **a,** ΔΦ as a function of time is plotted for various target potential differences. Data corresponding to 0.25 V, 0.75 V, 1.25 V, and 1.5 V were excluded during the MLFF training to validate the transferability of the model. Averaged lines are displayed as a thicker curve after applying a 2.5 ps moving average. Data corresponding to 0.25 V, 0.75 V, 1.25 V, and 1.5 V were excluded during the MLFF training and are therefore labeled as "untrained" in the legend. **b,**

Zoomed-in plot of ΔΦ versus time, focusing on the transient response. The horizontal arrows indicate the convergence time τ_Φ for the various target potentials.

Charging dynamics and electrolyte response

Applying a potential induces electrode charging, the fundamental mechanism that accelerates reaction kinetics in electrocatalysis or drives ion transport in electrochemical energy storage devices[49]. Therefore, the charging dynamics were analyzed by quantifying the surface charge density (σ) at each electrode (Figure 4a). Two distinct phases of polarization were observed. Below $\Delta\Phi = 0.5$ V, the interface was minimally polarized, showing σ of nearly 0.0 μC cm^{-2} at each electrode. While σ remains near zero, its subtle rearrangements at the interface, together with water responses, collectively contribute to the total interfacial potential, resulting in the stabilized ΔΦ (Figure S8). Detailed mechanisms regarding the water response will be discussed in following paragraphs. Above $\Delta\Phi = 0.5$ V, the interface became significantly polarized, with σ increasing gradually from −11 to −14 μC cm^{-2} as ΔΦ increased. The differential capacitance was determined to be 4 μF cm^{-2}, yielding a dielectric constant of less than 5 based on the classical capacitor model. This result aligns with previous findings regarding the restricted dielectric response of water at sub-nanoscale interfaces[24,25]. The timescale of electrode charging, τ_σ, was consistent with τ_Φ (Figure 4b). Specifically, τ_σ was nearly zero below $\Delta\Phi = 0.5$ V, while a decaying trend from 2 ps to 1 ps was observed at potentials above $\Delta\Phi = 0.5$ V.

At $\Delta\Phi = 0.5$ V, the system exhibited two distinct σ depending on the timescale. Up to $t = \tau_{\sigma,1}$, σ remained nearly zero, but it reached -10 μC cm^{-2} after $t = \tau_{\sigma,1} + \tau_{\sigma,2}$. The convergence timescales for σ (i.e., $\tau_{\sigma,1}$ and $\tau_{\sigma,2}$) and Φ (i.e., $\tau_{\Phi,1}$ and $\tau_{\Phi,2}$) were found to match. Specifically, $\tau_{\sigma,1}$ and $\tau_{\sigma,2}$ were measured as 4 ps and 2 ps, respectively. This indicates that the observed fluctuations in the μVT ensemble at $\Delta\Phi = 0.5$ V are ascribed to the transition between two distinct σ states, occurring within 2 ps. The existence of two distinct σ states at the same $\Delta\Phi$ was, in fact, predicted using a constant charge ensemble[3]. This suggests that multiple σ states can produce the same $\Delta\Phi$ because the electrolyte screens the electric field strongly at high external potentials but weakly at lower potentials, thereby maintaining a consistent potential drop. This mechanism explains the origin of the interfacial capacitance peak observed experimentally in dilute electrolytes, a behavior driven by the response of water molecules that can be applied analogously to explain the findings in this study. While the highly polarized interface with σ as -10 μC cm^{-2} shows a longer timescale owing to enthalpic gains from electrostatic interactions, this relationship must be system-size dependent to account for competing entropic effects. To the best of our knowledge, this is the first study to validate such predictions.

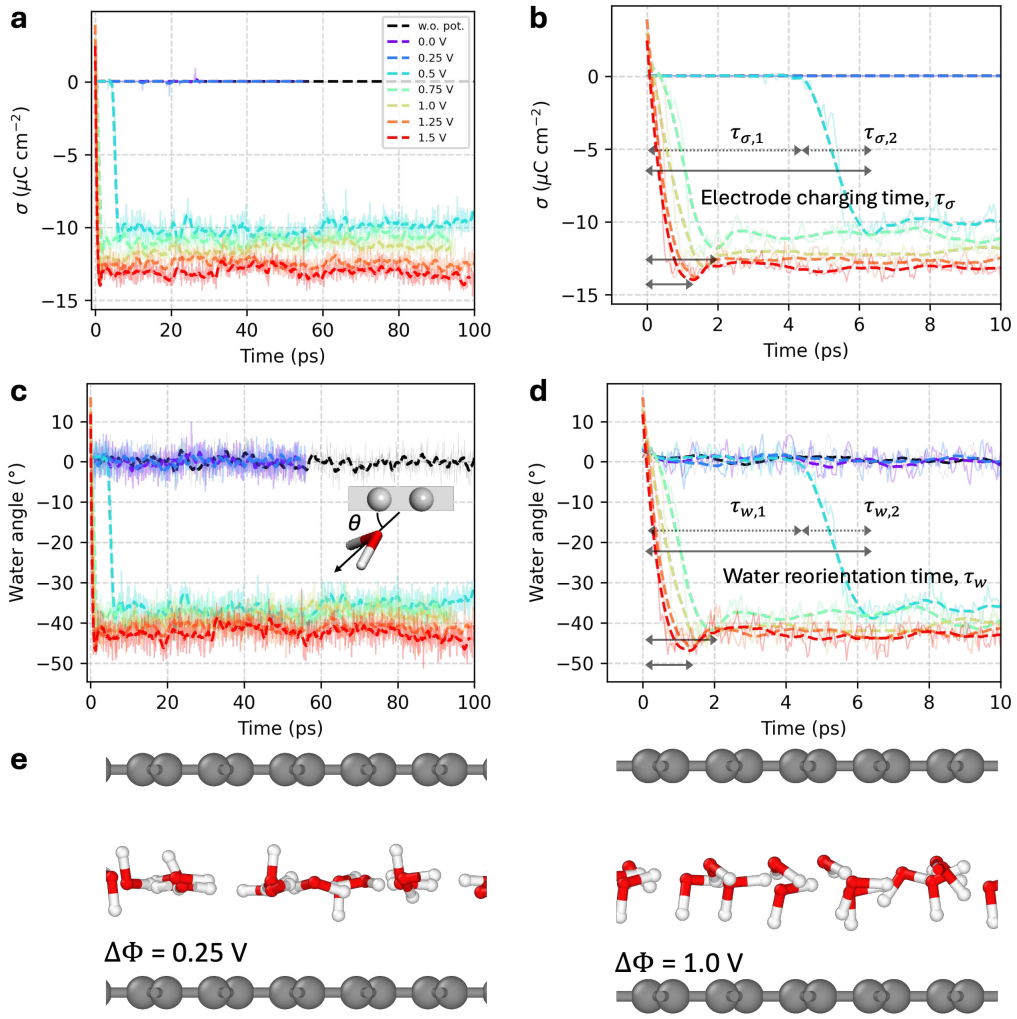


Figure 4. **a, b,** σ of the working electrode as a function of time under various ΔΦ conditions (**a**) and its zoomed-in image focusing on the transient response (**b**). **c, d,** The average orientation angle of water molecules as a function of time under various ΔΦ conditions (**c**) and its zoomed-in image focusing on the transient response (**d**). The horizontal arrows indicate the τ_σ, and τ_w for the various target potentials. The angle is defined as that between the vector connecting the oxygen atom to the midpoint of the hydrogen atoms and the electrode surface. **e,** A snapshot during the multiscale QM/ML simulation at ΔΦ is 0.25 V and 1.0 V.

The electrolyte response shows a strong correlation with electrode charging (Figures 4c, 4d and Figure S9). To quantify this, the average rotational angle of the water molecules was employed as the order parameter. Below $\Delta\Phi$ = 0.5 V, the average angle remained nearly 0°, exhibiting a randomized configuration (Figure 4e and Figure S10), and converged almost instantaneously, resulting in an electrolyte response timescale, τ_w, of approximately zero. Above $\Delta\Phi$ = 0.5 V, the angle shifted gradually from –50° to –60°, reflecting an oriented configuration to screen the electric field, with τ_w exhibiting a decreasing trend from 2 ps to 1 ps. At $\Delta\Phi$ = 0.5 V, two distinct timescales were identified: $\tau_{w,1}$ and $\tau_{w,2}$ as 4 ps and 2 ps, respectively. All measured timescales of the electrolyte response are consistent with those of the charging dynamics. Furthermore, the variation in σ is found to correlate with the number of adsorbed water molecules on the electrode (Figure S11), consistent with the previous observation from Pt electrode[10]. The number of hydrogen bonds decreases at $\Delta\Phi$ > 0.5 V to effectively screen the electric field in agreement with previous studies[3,9] (Figure S12).

In the monolayer, the limited configurational microstates of the electrolyte prevents a smooth response to external potentials. Beyond a specific threshold, the system undergoes drastic molecular rotations to accommodate the target $\Delta\Phi$, which leads to discontinuous changes in σ. While incorporating a polarizable force field might slightly mitigate this effect, it cannot fully compensate for the restricted phase space inherent in the monolayer[50]. The length scale where these anomalous signals were captured aligns well with previous studies, which identify restricted water motion with a critical threshold of 1 nm in confined spaces[24,25]. While existing literature primarily attributes this behavior to solid-surface interactions and spatial confinement, our results further suggest that the lack of configurational entropy is one underlying mechanism of this

suppressed flexibility. Our findings also align with previous constant-potential AIMD study[18], where potential convergence occurred within 4 ps, consistent with our observations. τ_σ was reported as 8 ps, attributed to the relatively slow response of the electrolyte within a system exceeding 10 water layers. Since there are more microstates of σ and electrolyte configurations that can yield the target ΔΦ, the convergence of σ can occur later than that of ΔΦ. This deviation is expected to be more prominent in the presence of ions, which significantly increase the configurational entropy.

The resulting μVT ensemble depends on the specific point-charge model employed in this architecture (Supplementary Note 2). While the electrolyte exhibits a consistent structural response under a constant external field, the magnitude of the potential drop varies across models. This discrepancy arises because each model yields a distinct total dipole moment for the same configuration, and the potentiostat functions differently within each model. Although these variations lead to distinct ensembles, they primarily cause a shift in the potential response. Specifically, more polarized models create a more polarized interface but with consistent capacitance, which leads to an earlier threshold without altering the fundamental physical message. These findings indicate the need for more rigorous future investigations using diverse charge sets. Additionally, such efforts should be complemented by experimental measurements once these methodologies are further developed and established, helping to identify an optimal model that reproduces the most realistic ensemble. Moreover, integrating polarizable models, such as the recently developed on-the-fly charge update schemes[36,40], is a promising direction for eliminating the sensitivity to fixed charge values in our methodology.

Transferability of the framework to more realistic electrochemical systems

We applied our methodological framework to various systems, including a larger bilayer distance system and varying ionic concentration conditions. This is intended to validate that our model is transferable to various electrochemical interface systems, which represent commonly used setups in previous computational electrochemistry studies[3,10,11,38]. Notably, no additional fine-tuning was performed for these systems, and the previously trained MLFF on the bulk electrolyte and monolayer model was reused, further demonstrating the transferability of our framework.

The first model employs a ~2 nm bilayer distance to analyze μVT ensemble, charging dynamics and electrolyte response with a more realistic system (Figure 5a). The μVT ensembles showed converged $\Delta\Phi$ as set, and tested up to 1.0 V (Figure 5b). The averaged $\Delta\Phi$ showed more than 0.5 V fluctuation without employing the potentiostat, further reinforcing the necessity of theoretical potentiostat. The τ_{Φ} is achieved on a relatively short timescale, on the order of a few picoseconds, consistent with the monolayer model and previous study[18].

Charging dynamics and electrolyte response still show a correlation with a quantitatively similar trend, with all signals appearing at nearly the same timescale (Figure 5c and 5d). Interestingly, τ_{σ} is significantly longer than τ_{Φ}, exceeding 25 ps when $\Delta\Phi \geq 0.5$ V. Both quantities exhibit persistent fluctuations following convergence, with σ fluctuating by $\pm$~3 μC cm^{-2} and water dipolar angle by $\pm$~3 °. This is consistent with previous research showing a deviation in the timescales required to achieve a constant potential and σ[18]. Since a thicker water layer has a larger degree of configurational freedom, it can produce diverse σ and water angle

within μVT ensembles, while ultimately converging to a stable configuration. Interestingly, however, when ΔΦ is 0.25 V, the system does not converge to a single value but instead exhibits a clear fluctuating trend between 0 and −10 μC cm^{-2}, further supporting the bistability of σ in μVT ensembles discussed in the monolayer model.

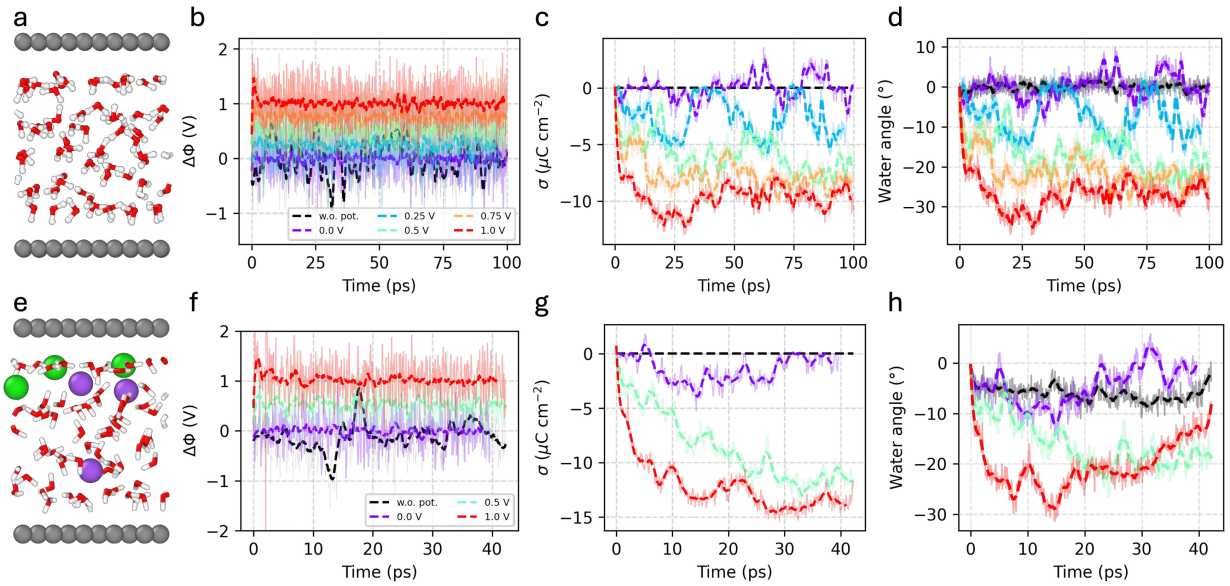


Figure 5. **a–d,** Constant potential QM/ML simulations with using ~2 nm bilayer graphene electrodes (a), to show ΔΦ (b), σ (c), water angle (d) as a function of time. **e–h,** the same analysis with employing 1 M NaCl electrolyte.

An ionic electrolyte is also incorporated into our theoretical framework using a 1 M NaCl solution (Figure 5e). ΔΦ shows convergence within a few picoseconds, but the averaged ΔΦ shows nearly 1 V fluctuation without employing the potentiostat (Figure 5f). The τ_σ is relatively similar to the pure water electrolyte timescale, i.e., > 20 ps, but the system is more strongly polarized, achieving a higher value of σ, e.g., approximately −15 μC cm^{-2} at −1.0 V compared

to −10 μC cm^{-2} in pure water system (Figure 5g). The interfacial capacitance for both cases falls within the range commonly measured experimentally[51]. However, unlike in the pure water system, the charging dynamics and averaged water angle no longer exhibit a clear one-to-one correlation, highlighting the importance of understanding ion dynamics in ionic systems (Figure 5h).

Moreover, we have shown that the approach remains valid at larger length scales over 5 nm (Supplementary Note 3), suggesting that it can be smoothly extended to more realistic electrochemical environments. We therefore envision this framework as a versatile tool for investigating a broad range of electrochemical phenomena, including reaction dynamics, interfacial reconstruction, and ion transport under applied potentials.

DISCUSSION

Computational electrochemistry faces two opposing demands: electronic-structure fidelity at the interface and access to long time- and length-scales for rare events and transport. Because no single method spans both, a multiscale strategy is required. We developed a QM/ML framework by coupling DFT for the electrode with an MLFF for the electrolyte; electrostatic embedding enables a computational potentiostat to maintain a target voltage.

This method provides deep insights into electrochemical interfaces at the sub-nanoscale—a regime where the interplay between electrode charging and electrolyte response at constant potential has been rarely explored due to prohibitive experimental limitations and computational challenges. Using a two-electrode graphene bilayer with monolayer water, we

generated μVT ensembles from 0 to 1.5 V in 0.25 V increments. While potentials converged within ~2 ps under a potentiostat, they fluctuated significantly without it, underlining the necessity of μVT sampling. Electrode charging and electrolyte response were strongly correlated, following the evolution of potential.

We extended our approach to more realistic electrochemical systems, including a larger bilayer distance model and a 1 M NaCl ionic electrolyte. The potential convergence timescale was comparable to that of the monolayer water system. The interfacial polarization timescale was significantly longer than that of the potential convergence attributed to the greater configurational entropy of the thicker electrolyte layer. The persistent bistability of surface charge density at low potential in the larger model further supports the findings from the monolayer model. In the ionic system, while the charging timescale remained similar, the electrolyte was more strongly polarized and the clear one-to-one correlation between charging dynamics and water orientation observed in pure water was no longer maintained, underscoring the distinct role of ion dynamics at electrochemical interfaces. Collectively, these results demonstrate the robustness and broad applicability of our framework across diverse electrochemical conditions.

Looking ahead, the full benefit of this framework will come from pairing constant-potential embedding with next-generation ML force fields that support dynamic charges and reactivity. Such models should be trained with active-learning loops and uncertainty quantification, so the potentiostat remains stable while the chemistry evolves. This will extend

fidelity to Faradaic events and interfacial reconstruction, and provide parameters directly to mesoscopic descriptions, closing a multiscale loop from electrons to devices.

METHODS

Theoretical framework of constant-potential QM/ML

The total Hamiltonian of the system is expressed as the sum of the following terms:

$$H_{QM/ML+potentiostat} = H_{QM} + H_{ML} + H_{interfacial} + H_{potentiostat} \quad (1).$$

The individual components are defined as:

$$H_{QM} = T_S[\rho] + \int dr\, V_{ext}(r)\rho(r) + E_H[\rho] + E_{XC}[\rho] \quad (2)$$

, where ρ is the electron density, T_s is kinetic energy, V_{ext} is nuclear potential, E_H is Hartree potential, and E_{XC} is exchange-correlation potential.

$$H_{ML} = \sum_i \frac{p_i^2}{2m_i} + U^{non-ES\ MLFF}(\{r_i\}) + \sum_{i\neq j} \frac{1}{2}\frac{q_i q_j}{|r_i - r_j|} \quad (3)$$

, where p_i, m_i, r_i, and q_i are the momentum, mass, position, and atomic charge of ML particles.

$$H_{potentiostat} = \int dr \frac{\Phi_{dev}}{1+\exp(-k(z-z_0))}\rho_{QM}(r) \quad (4)$$

, where Φ_{dev} is the deviated electrode potential from the target value, k is the steepness constant, and z_0 is the reference position.

$$H_{interfacial} = H_{interfacial\ ES} + U^{non-ES\ MLFF}(\{r_i\}, \{R_\mu\}) \quad (5)$$

, where $H_{interfacial\ ES}$ is the electrostatic interaction energy between ML and QM particles, r_i and R_μ are the positions of ML particles and QM particles. The interfacial ES Hamiltonian is defined differently for the QM and ML sectors to account for the electrostatic potential of counterpart:

$$H_{interfacial\ ES\ during\ QM} = \int dr V_{ML}(r)\rho_{QM}(r) \quad (6)$$

$$H_{interfacial\ ES\ during\ ML} = \int dr V_{QM}(r) \sum_i q_i \delta(r - \mathrm{r}_i) \quad (7)$$

, where the $V_{ML/QM}$ represent the electrostatic potential achieved after ML or QM, respectively. To practically implement this coupling, we solve Poisson's equation on a real-space grid. From ML to QM, to obtain the charge density from the ML, the ML runs for 50 fs, and the charge density $\rho_{ML}(r)$ is averaged and saved in a three-dimensional real-space grid exact format corresponding to the QM grid:

$$\rho_{ML}(r) = \frac{1}{\tau} \int_{t=0}^{\tau} dt \sum_i q_i \delta(r - \mathrm{r}_i(t)) \quad (8)$$

, where τ is the ML running timescale set as 50 fs for this work. The electrostatic potential is then derived by solving:

$$\nabla^2 V_{ML}(r) = -4\pi \rho_{ML}(r) \quad (9).$$

The QM calculation directly incorporates this potential using a specific module in CP2K that reads external potential files. From QM to ML, similarly, the potential produced by the QM electron density is solved via:

$$\nabla^2 V_{QM}(r) = -4\pi \rho_{QM}(r) \quad (10).$$

The ML simulation reads this potential file, ensuring that the potential acting on the ML particles is exactly the same as that produced by the QM calculation. It has been validated in previous works and is publicly available in our GitHub repository[42].

The process for extracting the non-ES energy is discussed here. The initial DFT dataset can be divided into ES and non-ES components, as follows:

$$H_{DFT} = H_{ES} + H_{non-ES} \quad (11).$$

Regarding the ES among the ML particles, since the system does not include QM particles, all charges are treated as point charges in this work. Consequently, the ES contribution is represented solely through point charge interactions. The non-ES term can therefore be expressed as follows:

$$H_{non-ES,ML} = H_{DFT} - \sum_{i \neq j} \frac{1}{2} \frac{q_i q_j}{|\mathbf{r}_i - \mathbf{r}_j|} \quad (12).$$

In the case of ES interactions between QM and ML particles, the ES contribution is defined by the interaction between the electrostatic potential from the electrode and the point charges of the ML particles. Consequently, the non-ES energy is represented as:

$$H_{non-ES,QM/ML} = H_{DFT} - \int dr V_{QM}(r) \sum_i q_i \delta(r - \mathrm{r}_i) \quad (13).$$

These non-ES datasets are collected to construct the training dataset for the MLFF development in this work.

Computational Details

DFT simulations were run using CP2K[52] with the generalized gradient approximation using the revPBE functional[53] and D3 dispersion correction.[54] This functional has been shown to accurately represent the structural and dynamic properties of liquid water[55–57] as well as water-graphene interaction energies.[58] The TZV2P basis set[59] and GTH pseudopotentials[60] were used for all electrolyte atoms, while carbon atoms were modeled with the short range DZVP basis set[59] and GTH pseudopotential.[60] A plane wave cutoff was 1200 Ry. The graphene layer has the lattice size of 12.35 Å and 12.84 Å with the slits packed at a density of approximately 1 g cm^{-3}. The main data are from when the slit height is 6.7 Å. It incorporates 17 water molecules arranged in a monolayer.

The machine learning potential developed in this work consists of a committee of seven Behler-Parrinello neural networks,[61–63] each containing two hidden layers with 20 nodes. Atom-centered symmetry functions[64] (ACSFs) with a cutoff of 12 Bohr are used to encode the

chemical environments of each atom. Ten radial symmetry functions and four angular symmetry functions are used to describe each two- and three-body grouping of atoms, respectively. The neural network parameters were optimized using the n2p2 code[65,66] with 100 epochs of training. To introduce variability between the seven committee members, 10% of structures were randomly selected for each committee and omitted from the training set.

The initial training dataset for the QM/ML model consisted of two sets of structures: bulk NaCl in water and confined structures with graphene sheets taken from previous work[37]. The bulk NaCl dataset comprises 1049 samples, containing 0, 1, 2, 3, or 4 NaCl ion pairs in water. The simulation box is nearly isotropic with a side length of 23.4 Å. The confined structure dataset includes 939 samples, featuring four different interlayer distances between graphene sheets: 6.7, 10.05, 13.4, and 16.75 Å. In these structures, the aqueous electrolyte incorporates various numbers of NaCl ion pairs, ranging from 0 to 3. For both datasets, point charges were assigned to the electrolyte atoms (SPC/E model for water molecules; ±1 for the Na^+ and Cl^-). For the confined structures, the electronic structure of graphene electrode was described with DFT. The electrostatic interaction between the electrode and electrolyte was calculated via real-space 3-dimensional grid using the module implemented in the DFT-CES package (https://github.com/SeungJay/DFT-CES). The training dataset is then prepared by subtracting all the electrostatic interactions from the DFT data to isolate the short-range interaction dominant dataset. Finally, for fine-tuning, potentiostat-coupled QM/ML simulation was conducted to achieve $\Delta\Phi$ values of 0.5 V and 1.0 V. From the trajectories generated via

QM/ML simulations, forty snapshots were randomly sampled at each potential. These snapshots were then subjected to DFT calculations, and the electrostatic contributions were decoupled, and the resulting non-ES data were subsequently merged into the next round of training.

The constant potential QM/ML simulations were performed using the LAMMPS interface of the n2p2 code and DFT-CES. Bespoke Python code was developed to iteratively run this with CP2K code. It is designed to synchronize the electrostatic potential across the interface by alternating between CP2K and LAMMPS, thereby generating a constant potential ensemble through the use of a potentiostat. The simulations were carried out to achieve μVT ensemble at 300 K maintained using a Nosé-Hoover style thermostat with a damping parameter of 100 fs. The equations of motion were integrated using the velocity Verlet algorithm based on the average prediction of all 7 network committee members, with a time step of 0.5 fs. The electrostatic interaction was calculated using 2-dimensional particle-particle particle-mesh (PPPM) method among the electrolyte particles,[67] and 3-dimensional grid-based interaction for the electrode-electrolyte parts. At every 50 fs, DFT calculation was conducted. The external potential module was employed to apply the electrostatic potential from the electrolyte component. Subsequently, following the measurement of the electrode potential, a sigmoid-shaped potential is applied to the electrodes to drive the potential difference ΔΦ toward the target value.

ASSOCIATED CONTENT

Data availability

The bespoke Python code for executing the QM/ML simulations is available at https://github.com/SeungJay/QM-ML-project. The datasets used for training the MLFF are also provided at the same repository.

Supporting Information

The Supporting Information is available free of charge.

- Validation of QM/ML results with DFT calculations, comparison of different point charge models, scalability of the constant potential QM/ML method, training and test results of the MLFF (S1–6), potential evolution versus time tracked after an ML run (S7), electrostatic potential profiles at 0.0 V and 0.25 V (S8), total electrolyte dipole moment evolution versus time (S9), snapshots of QM/ML simulations (S10), correlation between adsorbed water molecules and surface charge density (S11), and hydrogen bond analysis (S12).

AUTHOR INFORMATION

Corresponding Author

Seung-Jae Shin – School of Energy and Chemical Engineering, Ulsan National Institute of Science and Technology (UNIST), Ulsan 44919, Republic of Korea

https://orcid.org/0000-0002-5530-4453; E-mail: seung-jae.shin@unist.ac.kr

Author Contributions

S.-J. Shin conceived the idea and conducted every training and development. A. Walsh advised the project. K. D. Fong contributed the initial dataset. All authors contributed to the analysis and writing of the manuscript.

Notes

The authors declare no competing financial interest.

ACKNOWLEDGMENT

This research was supported by the National Research Foundation of Korea (NRF) funded by Ministry of Science and ICT (RS-2025-25442300 and RS-2026-25489675), the Technology Innovation Program (RS-2025-25463205) funded by the Ministry of Trade Industry & Resources (MOTIR, Korea), and innoCore program of the Ministry of Science and ICT (1.260005.01). We acknowledge the support of the Korea Institute of Science and Technology Information (KISTI) National Supercomputing Center with supercomputing resources, including technical support (KSC-2024-CRE-0429 and KSC-2025-CRE-0567), and the supercomputing resources of the UNIST Supercomputing Center. This work was also supported by EPSRC project EP/X037754/1 and via our membership of the UK's HEC Materials Chemistry Consortium, which is funded by EPSRC (EP/X035859/1), the ARCHER2 UK National Supercomputing Service (http://www.archer2.ac.uk) was used. KDF acknowledges

support from Schmidt Science Fellows, in partnership with the Rhodes Trust, and Trinity College, Cambridge.

REFERENCES

(1) Seh, Z. W.; Kibsgaard, J.; Dickens, C. F.; Chorkendorff, I.; Nørskov, J. K.; Jaramillo, T. F. Combining Theory and Experiment in Electrocatalysis: Insights into Materials Design. *Science* **2017**, *355* (6321), eaad4998. https://doi.org/10.1126/science.aad4998.

(2) Nørskov, J. K.; Rossmeisl, J.; Logadottir, A.; Lindqvist, L.; Kitchin, J. R.; Bligaard, T.; Jónsson, H. Origin of the Overpotential for Oxygen Reduction at a Fuel-Cell Cathode. *J. Phys. Chem. B* **2004**, *108* (46), 17886–17892. https://doi.org/10.1021/jp047349j.

(3) Shin, S.-J.; Kim, D. H.; Bae, G.; Ringe, S.; Choi, H.; Lim, H.-K.; Choi, C. H.; Kim, H. On the Importance of the Electric Double Layer Structure in Aqueous Electrocatalysis. *Nat. Commun.* **2022**, *13* (1), 174. https://doi.org/10.1038/s41467-021-27909-x.

(4) Ringe, S. The Importance of a Charge Transfer Descriptor for Screening Potential CO2 Reduction Electrocatalysts. *Nat. Commun.* **2023**, *14* (1), 2598. https://doi.org/10.1038/s41467-023-37929-4.

(5) Monteiro, M. C. O.; Dattila, F.; Hagedoorn, B.; García-Muelas, R.; López, N.; Koper, M. T. M. Absence of CO2 Electroreduction on Copper, Gold and Silver Electrodes without Metal Cations in Solution. *Nat. Catal.* **2021**, *4* (8), 654–662. https://doi.org/10.1038/s41929-021-00655-5.

(6) Li, L.; Reuter, K.; Hörmann, N. G. Deciphering the Capacitance of the Pt(111)/Water Interface: A Micro- to Mesoscopic Investigation by AIMD and Implicit Solvation. *ACS Electrochem.* **2025**, *1* (2), 186–194. https://doi.org/10.1021/acselectrochem.4c00062.

(7) Zhen, E.; Chen, Y.; Huang, J. Double-Layer Capacitance Peaks: Origins, Ion Dependence, and Temperature Effects. *J. Chem. Phys.* **2025**, *162* (14), 144702. https://doi.org/10.1063/5.0251548.

(8) Li, L.; Eggert, T.; Reuter, K.; Hörmann, N. G. Electron Spillover into Water Layers: A Quantum Leap in Understanding Capacitance Behavior. *J. Am. Chem. Soc.* **2025**, *147* (26), 22778–22784. https://doi.org/10.1021/jacs.5c04728.

(9) Li, C.-Y.; Le, J.-B.; Wang, Y.-H.; Chen, S.; Yang, Z.-L.; Li, J.-F.; Cheng, J.; Tian, Z.-Q. In Situ Probing Electrified Interfacial Water Structures at Atomically Flat Surfaces. *Nat. Mater.* **2019**, *18* (7), 697–701. https://doi.org/10.1038/s41563-019-0356-x.

(10) Le, J.-B.; Fan, Q.-Y.; Li, J.-Q.; Cheng, J. Molecular Origin of Negative Component of Helmholtz Capacitance at Electrified Pt(111)/Water Interface. *Sci. Adv.* **2020**, *6* (41), eabb1219. https://doi.org/10.1126/sciadv.abb1219.

(11) Shin, S.-J.; Choi, H.; Ringe, S.; Won, D. H.; Oh, H.-S.; Kim, D. H.; Lee, T.; Nam, D.-H.; Kim, H.; Choi, C. H. A Unifying Mechanism for Cation Effect Modulating C1 and C2

Productions from CO_2 Electroreduction. *Nat. Commun.* **2022**, *13* (1), 5482. https://doi.org/10.1038/s41467-022-33199-8.
(12) Shin, S.-J.; Gittins, J. W.; Golomb, M. J.; Forse, A. C.; Walsh, A. Microscopic Origin of Electrochemical Capacitance in Metal–Organic Frameworks. *J. Am. Chem. Soc.* **2023**, *145* (26), 14529–14538. https://doi.org/10.1021/jacs.3c04625.
(13) Unke, O. T.; Chmiela, S.; Sauceda, H. E.; Gastegger, M.; Poltavsky, I.; Schütt, K. T.; Tkatchenko, A.; Müller, K.-R. Machine Learning Force Fields. *Chem. Rev.* **2021**, *121* (16), 10142–10186. https://doi.org/10.1021/acs.chemrev.0c01111.
(14) Sundararaman, R.; Goddard, W. A., III; Arias, T. A. Grand Canonical Electronic Density-Functional Theory: Algorithms and Applications to Electrochemistry. *J. Chem. Phys.* **2017**, *146* (11), 114104. https://doi.org/10.1063/1.4978411.
(15) Chai, Z.; Luber, S. Grand Canonical Ensemble Approaches in CP2K for Modeling Electrochemistry at Constant Electrode Potentials. *J. Chem. Theory Comput.* **2024**, *20* (18), 8214–8228. https://doi.org/10.1021/acs.jctc.4c00671.
(16) Siepmann, J. I.; Sprik, M. Influence of Surface Topology and Electrostatic Potential on Water/Electrode Systems. *J. Chem. Phys.* **1995**, *102* (1), 511–524. https://doi.org/10.1063/1.469429.
(17) Deißenbeck, F.; Freysoldt, C.; Todorova, M.; Neugebauer, J.; Wippermann, S. Dielectric Properties of Nanoconfined Water: A Canonical Thermopotentiostat Approach. *Phys. Rev. Lett.* **2021**, *126* (13), 136803. https://doi.org/10.1103/PhysRevLett.126.136803.
(18) Deißenbeck, F.; Wippermann, S. Dielectric Properties of Nanoconfined Water from Ab Initio Thermopotentiostat Molecular Dynamics. *J. Chem. Theory Comput.* **2023**, *19* (3), 1035–1043. https://doi.org/10.1021/acs.jctc.2c00959.
(19) VahidMohammadi, A.; Rosen, J.; Gogotsi, Y. The World of Two-Dimensional Carbides and Nitrides (MXenes). *Science* **2021**, *372* (6547), eabf1581. https://doi.org/10.1126/science.abf1581.
(20) Gouy, M. Sur la constitution de la charge électrique à la surface d'un électrolyte. *J. Phys.: Theor. Appl.* **1910**, *9* (1), 457–468. https://doi.org/10.1051/jphystap:019100090045700.
(21) Chapman, D. L. LI. A Contribution to the Theory of Electrocapillarity. *London Edinburgh Philos. Mag. J. Sci.* **1913**, *25* (148), 475–481. https://doi.org/10.1080/14786440408634187.
(22) Stern, O. Zur theorie der elektrolytischen doppelschicht. *Zeit. Elektrochem.* **1924**, *30*, 508–516.
(23) Wang, Y.; Tang, F.; Yu, X.; Chiang, K.-Y.; Yu, C.-C.; Ohto, T.; Chen, Y.; Nagata, Y.; Bonn, M. Interfaces Govern the Structure of Angstrom-Scale Confined Water Solutions. *Nat. Commun.* **2025**, *16* (1), 7288. https://doi.org/10.1038/s41467-025-62625-w.
(24) Fumagalli, L.; Esfandiar, A.; Fabregas, R.; Hu, S.; Ares, P.; Janardanan, A.; Yang, Q.; Radha, B.; Taniguchi, T.; Watanabe, K.; Gomila, G.; Novoselov, K. S.; Geim, A. K. Anomalously Low Dielectric Constant of Confined Water. *Science* **2018**, *360* (6395), 1339–1342. https://doi.org/10.1126/science.aat4191.

(25) Gopinadhan, K.; Hu, S.; Esfandiar, A.; Lozada-Hidalgo, M.; Wang, F. C.; Yang, Q.; Tyurnina, A. V.; Keerthi, A.; Radha, B.; Geim, A. K. Complete Steric Exclusion of Ions and Proton Transport through Confined Monolayer Water. *Science* **2019**, *363* (6423), 145–148. https://doi.org/10.1126/science.aau6771.

(26) Wang, R.; Souilamas, M.; Esfandiar, A.; Fabregas, R.; Benaglia, S.; Nevison-Andrews, H.; Yang, Q.; Normansell, J.; Ares, P.; Ferrari, G.; Principi, A.; Geim, A. K.; Fumagalli, L. In-Plane Dielectric Constant and Conductivity of Confined Water. *Nature* **2025**, *646* (8085), 606–610. https://doi.org/10.1038/s41586-025-09558-y.

(27) King, D. S.; Kim, D.; Zhong, P.; Cheng, B. Machine Learning of Charges and Long-Range Interactions from Energies and Forces. *Nat. Commun.* **2025**, *16* (1), 8763. https://doi.org/10.1038/s41467-025-63852-x.

(28) Sun, Q.; Chan, G. K.-L. Quantum Embedding Theories. *Acc. Chem. Res.* **2016**, *49* (12), 2705–2712. https://doi.org/10.1021/acs.accounts.6b00356.

(29) Kovács, D. P.; Moore, J. H.; Browning, N. J.; Batatia, I.; Horton, J. T.; Pu, Y.; Kapil, V.; Witt, W. C.; Magdău, I.-B.; Cole, D. J.; Csányi, G. MACE-OFF: Short-Range Transferable Machine Learning Force Fields for Organic Molecules. *J. Am. Chem. Soc.* **2025**, *147* (21), 17598–17611. https://doi.org/10.1021/jacs.4c07099.

(30) Cheng, B. Latent Ewald Summation for Machine Learning of Long-Range Interactions. *npj Comput. Mater.* **2025**, *11* (1), 80. https://doi.org/10.1038/s41524-025-01577-7.

(31) Jorgensen, W. L.; Maxwell, D. S.; Tirado-Rives, J. Development and Testing of the OPLS All-Atom Force Field on Conformational Energetics and Properties of Organic Liquids. *J. Am. Chem. Soc.* **1996**, *118* (45), 11225–11236. https://doi.org/10.1021/ja9621760.

(32) Foiles, S. M.; Baskes, M. I.; Daw, M. S. Embedded-Atom-Method Functions for the Fcc Metals Cu, Ag, Au, Ni, Pd, Pt, and Their Alloys. *Physical Review B* **1986**, *33* (12), 7983–7991. https://doi.org/10.1103/PhysRevB.33.7983.

(33) Bard, A. J.; Faulkner, L. R. Potentials and Thermodynamics of Cells. In *Electrochemical Methods: Fundamentals and Applications*, 2nd ed.; John Wiley & Sons, Inc., 2001.

(34) Jerkiewicz, G. Standard and Reversible Hydrogen Electrodes: Theory, Design, Operation, and Applications. *ACS Catal.* **2020**, *10* (15), 8409–8417. https://doi.org/10.1021/acscatal.0c02046.

(35) Lim, H.-K.; Lee, H.; Kim, H. A Seamless Grid-Based Interface for Mean-Field QM/MM Coupled with Efficient Solvation Free Energy Calculations. *J. Chem. Theory Comput.* **2016**, *12* (10), 5088–5099. https://doi.org/10.1021/acs.jctc.6b00469.

(36) Behler, J. Four Generations of High-Dimensional Neural Network Potentials. *Chem. Rev.* **2021**, *121* (16), 10037–10072. https://doi.org/10.1021/acs.chemrev.0c00868.

(37) Fong, K. D.; Sumić, B.; O'Neill, N.; Schran, C.; Grey, C. P.; Michaelides, A. The Interplay of Solvation and Polarization Effects on Ion Pairing in Nanoconfined Electrolytes. *Nano Lett.* **2024**, *24* (16), 5024–5030. https://doi.org/10.1021/acs.nanolett.4c00890.

(38) Kim, M. M.; Kim, D. H.; Cho, J.; Shin, S.-J.; Choi, C. H.; Kim, H. Electric Double Layer Structure in Concentrated Aqueous Solution. *Nat Commun* **2026**. https://doi.org/10.1038/s41467-026-70322-5.
(39) Advincula, X. R.; Fong, K. D.; Wang, Y.; Schran, C.; Bonn, M.; Michaelides, A.; Litman, Y. Breaking the Air–Water Paradigm: Ion Behavior at Hydrophobic Solid–Water Interfaces. *J. Am. Chem. Soc.* **2026**. https://doi.org/10.1021/jacs.5c20209.
(40) Cheng, B. Latent Ewald Summation for Machine Learning of Long-Range Interactions. *npj Comput. Mater.* **2025**, *11* (1), 80. https://doi.org/10.1038/s41524-025-01577-7.
(41) Zhu, J.-X.; Cheng, J. Machine Learning Potential for Electrochemical Interfaces with Hybrid Representation of Dielectric Response. *Phys. Rev. Lett.* **2025**, *135* (1), 018003. https://doi.org/10.1103/48ct-3jxm.
(42) Shin, S.-J. SeungJay/DFT-CES, 2025. https://github.com/SeungJay/DFT-CES.
(43) van de Ven, G. M.; Soures, N.; Kudithipudi, D. 1.09 - Continual Learning and Catastrophic Forgetting. In *Learning and Memory: A Comprehensive Reference (Third Edition)*; Wixted, J., Ed.; Academic Press: Oxford, 2025; pp 153–168. https://doi.org/10.1016/B978-0-443-15754-7.00073-0.
(44) Advincula, X. R.; Fong, K. D.; Michaelides, A.; Schran, C. Protons Accumulate at the Graphene–Water Interface. *ACS Nano* **2025**, *19* (18), 17728–17737. https://doi.org/10.1021/acsnano.5c02053.
(45) Litman, Y.; Michaelides, A. Entropy Governs the Structure and Reactivity of Water Dissociation Under Electric Fields. *J. Am. Chem. Soc.* **2025**. https://doi.org/10.1021/jacs.5c12397.
(46) Hoover, W. G. Canonical Dynamics: Equilibrium Phase-Space Distributions. *Phys. Rev. A* **1985**, *31* (3), 1695–1697. https://doi.org/10.1103/PhysRevA.31.1695.
(47) Melchionna, S.; Ciccotti, G.; Lee Holian, B. Hoover *NPT* Dynamics for Systems Varying in Shape and Size. *Molecular Physics* **1993**, *78* (3), 533–544. https://doi.org/10.1080/00268979300100371.
(48) Nosé, S. A Unified Formulation of the Constant Temperature Molecular Dynamics Methods. *The Journal of Chemical Physics* **1984**, *81* (1), 511–519. https://doi.org/10.1063/1.447334.
(49) Bard, A. J.; Faulkner, L. R. Kinetics of Electrode Reactions. In *Electrochemical Methods: Fundamentals and Applications*, 2nd ed.; John Wiley & Sons, Inc., 2001.
(50) Bedrov, D.; Piquemal, J.-P.; Borodin, O.; MacKerell, A. D. Jr.; Roux, B.; Schröder, C. Molecular Dynamics Simulations of Ionic Liquids and Electrolytes Using Polarizable Force Fields. *Chem. Rev.* **2019**, *119* (13), 7940–7995. https://doi.org/10.1021/acs.chemrev.8b00763.
(51) Ji, H.; Zhao, X.; Qiao, Z.; Jung, J.; Zhu, Y.; Lu, Y.; Zhang, L. L.; MacDonald, A. H.; Ruoff, R. S. Capacitance of Carbon-Based Electrical Double-Layer Capacitors. *Nat. Commun.* **2014**, *5* (1), 3317. https://doi.org/10.1038/ncomms4317.
(52) Kühne, T. D.; Iannuzzi, M.; Del Ben, M.; Rybkin, V. V.; Seewald, P.; Stein, F.; Laino, T.; Khaliullin, R. Z.; Schütt, O.; Schiffmann, F.; Golze, D.; Wilhelm, J.; Chulkov, S.; Bani-

Hashemian, M. H.; Weber, V.; Borštnik, U.; Taillefumier, M.; Jakobovits, A. S.; Lazzaro, A.; Pabst, H.; Müller, T.; Schade, R.; Guidon, M.; Andermatt, S.; Holmberg, N.; Schenter, G. K.; Hehn, A.; Bussy, A.; Belleflamme, F.; Tabacchi, G.; Glöß, A.; Lass, M.; Bethune, I.; Mundy, C. J.; Plessl, C.; Watkins, M.; VandeVondele, J.; Krack, M.; Hutter, J. CP2K: An Electronic Structure and Molecular Dynamics Software Package - Quickstep: Efficient and Accurate Electronic Structure Calculations. *The Journal of Chemical Physics* **2020**, *152* (19), 194103. https://doi.org/10.1063/5.0007045.

(53) Perdew, J. P.; Burke, K.; Ernzerhof, M. Generalized Gradient Approximation Made Simple. *Phys. Rev. Lett.* **1996**, *77* (18), 3865–3868. https://doi.org/10.1103/PhysRevLett.77.3865.

(54) Grimme, S.; Antony, J.; Ehrlich, S.; Krieg, H. A Consistent and Accurate Ab Initio Parametrization of Density Functional Dispersion Correction (DFT-D) for the 94 Elements H-Pu. *J. Chem. Phys.* **2010**, *132* (15), 154104. https://doi.org/10.1063/1.3382344.

(55) Morawietz, T.; Singraber, A.; Dellago, C.; Behler, J. How van Der Waals Interactions Determine the Unique Properties of Water. *Proceedings of the National Academy of Sciences* **2016**, *113* (30), 8368–8373. https://doi.org/10.1073/pnas.1602375113.

(56) Gillan, M. J.; Alfè, D.; Michaelides, A. Perspective: How Good Is DFT for Water? *J. Chem. Phys.* **2016**, *144* (13), 130901. https://doi.org/10.1063/1.4944633.

(57) Marsalek, O.; Markland, T. E. Quantum Dynamics and Spectroscopy of Ab Initio Liquid Water: The Interplay of Nuclear and Electronic Quantum Effects. *J. Phys. Chem. Lett.* **2017**, *8* (7), 1545–1551. https://doi.org/10.1021/acs.jpclett.7b00391.

(58) Brandenburg, J. G.; Zen, A.; Alfè, D.; Michaelides, A. Interaction between Water and Carbon Nanostructures: How Good Are Current Density Functional Approximations? *J. Chem. Phys.* **2019**, *151* (16), 164702. https://doi.org/10.1063/1.5121370.

(59) VandeVondele, J.; Hutter, J. Gaussian Basis Sets for Accurate Calculations on Molecular Systems in Gas and Condensed Phases. *J. Chem. Phys.* **2007**, *127* (11), 114105. https://doi.org/10.1063/1.2770708.

(60) Goedecker, S. Separable Dual-Space Gaussian Pseudopotentials. *Phys. Rev. B* **1996**, *54* (3), 1703–1710. https://doi.org/10.1103/PhysRevB.54.1703.

(61) Behler, J. Generalized Neural-Network Representation of High-Dimensional Potential-Energy Surfaces. *Phys. Rev. Lett.* **2007**, *98* (14). https://doi.org/10.1103/PhysRevLett.98.146401.

(62) Behler, J. Four Generations of High-Dimensional Neural Network Potentials. *Chem. Rev.* **2021**, *121* (16), 10037–10072. https://doi.org/10.1021/acs.chemrev.0c00868.

(63) Schran, C.; Brezina, K.; Marsalek, O. Committee Neural Network Potentials Control Generalization Errors and Enable Active Learning. *J. Chem. Phys.* **2020**, *153* (10), 104105. https://doi.org/10.1063/5.0016004.

(64) Behler, J. Atom-Centered Symmetry Functions for Constructing High-Dimensional Neural Network Potentials. *J. Chem. Phys.* **2011**, *134* (7), 074106. https://doi.org/10.1063/1.3553717.

(65) Singraber, A.; Morawietz, T.; Behler, J.; Dellago, C. Parallel Multistream Training of High-Dimensional Neural Network Potentials. *J. Chem. Theory Comput.* **2019**, *15* (5), 3075–3092. https://doi.org/10.1021/acs.jctc.8b01092.
(66) Singraber, A.; Behler, J.; Dellago, C. Library-Based LAMMPS Implementation of High-Dimensional Neural Network Potentials. *J. Chem. Theory Comput.* **2019**, *15* (3), 1827–1840. https://doi.org/10.1021/acs.jctc.8b00770.
(67) Yeh, I.-C.; Berkowitz, M. L. Ewald Summation for Systems with Slab Geometry. *J. Chem. Phys.* **1999**, *111* (7), 3155–3162. https://doi.org/10.1063/1.479595.

Supplementary Files

This is a list of supplementary files associated with this preprint. Click to download.

- SupportingInformation.pdf